Railway Engineering Science (2024) 32(2):194–210
https://doi.org/10.1007/s40534-023-00325-1

Computer vision-aided DEM study on the compaction characteristics of graded subgrade filler considering realistic coarse particle shapes

Taifeng Li[1] · Kang Xie[2,3] · Xiaobin Chen[2] · Zhixing Deng[2,3] · Qian Su[3]

Received: 25 April 2023 / Revised: 20 October 2023 / Accepted: 25 October 2023 / Published online: 8 December 2023

Abstract
The compaction quality of subgrade filler strongly affects subgrade settlement. The main objective of this research is to analyze the macro- and micro-mechanical compaction characteristics of subgrade filler based on the real shape of coarse particles. First, an improved Viola–Jones algorithm is employed to establish a digitalized 2D particle database for coarse particle shape evaluation and discrete modeling purposes of subgrade filler. Shape indexes of 2D subgrade filler are then computed and statistically analyzed. Finally, numerical simulations are performed to quantitatively investigate the effects of the aspect ratio (AR) and interparticle friction coefficient (μ) on the macro- and micro-mechanical compaction characteristics of subgrade filler based on the discrete element method (DEM). The results show that with the increasing AR, the coarse particles are narrower, leading to the increasing movement of fine particles during compaction, which indicates that it is difficult for slender coarse particles to inhibit the migration of fine particles. Moreover, the average displacement of particles is strongly influenced by the AR, indicating that their occlusion under power relies on particle shapes. The displacement and velocity of fine particles are much greater than those of the coarse particles, which shows that compaction is primarily a migration of fine particles. Under the cyclic load, the interparticle friction coefficient μ has little effect on the internal structure of the sample; under the quasi-static loads, however, the increase in μ will lead to a significant increase in the porosity of the sample. This study could not only provide a novel approach to investigate the compaction mechanism but also establish a new theoretical basis for the evaluation of intelligent subgrade compaction.

Keywords Subgrade filler particles · Deep learning particle · Shape analysis · Particle library · Compaction characteristics · Discrete element method (DEM)

1 Introduction

The compaction quality of filler is an important factor controlling the settlement and deformation of subgrade structures [1, 2], and it will affect the long-term stability and safe operation of high-speed railway subgrade [3–5]. The compaction process mainly changes the skeleton structure and arrangement of the filler, promotes the active relative displacement between the particles in the soil, and forms the filler with a compact texture, to meet the mechanical characteristics of the high-speed railway subgrade [6, 7]. Therefore, understanding the particle movement law and compaction characteristics of the filler is the key to compaction control, and there is an urgent need to strictly control the compaction quality of coarse-grained soil filler [8, 9].

The existing studies on the compaction characteristics of coarse-grained soil filler (including static and vibration compaction) have focused on macroscopic behaviors and fall into two categories: (1) using laboratory tests to investigate the effect of compaction parameters [10, 11], particle gradation [12–17], and fine particle content [18, 19] on the compaction characteristics of coarse-grained soil and (2) using field tests to explore the vibration response characteristics of the machine–soil coupling system and filler, with some indicators proposed to reflect the subgrade compaction quality [20–23]. However, during the

✉ Kang Xie
xiekang1995@csu.edu.cn

[1] Railway Engineering Research Institute, China Academy of Railway Sciences Corporation Limited, Beijing 100081, China

[2] Department of Civil Engineering, Central South University, Changsha 410075, China

[3] School of Civil Engineering, Southwest Jiaotong University, Chengdu 610031, China

compaction process of coarse-grained soil filler, the evolution of mesostructure and contact characteristics is difficult to accurately analyze through laboratory tests. To better achieve compaction quality control, the evolution of the internal microstructure of coarse-grained soil filler during the compaction process and the relationship between the macroscopic state and microscopic indicators need to be studied in depth.

Nowadays, numerical simulation has become a common way to study mechanical properties of coarse-grained soil filler [24–27], and much research are devoted to the compaction characteristics and mechanical response of coarse-grained soils via discrete element method (DEM) [28, 29]. However, these research adopts spherical particles for simulation, which cannot reflect the real particle motion. The strength and deformation of the coarse-grained soil filler are closely dependent on the particle shapes [30–33]. Therefore, it is of great significance to consider the influence of particle morphology on the compaction mechanism of coarse-grained soil filler. Particle contour acquisition is a prerequisite for particle morphology analysis. Since the end of the last century, Mora et al. [34], Fernlund [35], and other scholars have adopted cameras to obtain particle contour information. Thus, multiple particle contours can be captured at once using a camera combined with an image processing technology. However, it is necessary to manually load and remove particles from trays repeatedly, resulting in a high workload and low efficiency, which limits the performance of this approach in batch analysis. To reduce the workload required for particle loading, many automated images acquisition (measurement) systems have been developed, such as WipShape [36], VDG40 videograder [37], and the aggregate imaging system (AIMS) [38]. However, the necessity for relatively complex and expensive equipment limits the application of the automated image acquisition system in projects. With the development of digital image processing (DIP) technology, scholars [34, 39, 40–46] have proposed automated DIP algorithms to extract particle contours from original particulate matter images, thereby reducing the dependence on complex equipment. The image acquisition method based on the DIP algorithm does not rely on the complex image-capturing equipment and directly post-processes the original image to obtain the particle outline, which significantly reduces the labor and equipment costs of image acquisition [42, 47]. Due to the complexity of the image texture, the postprocessing process still requires manual intervention, which limits the efficiency of this method in the batch analysis [48, 49]. Therefore, developing a method suitable for particle morphology analysis that directly extracts and separates particle contours from

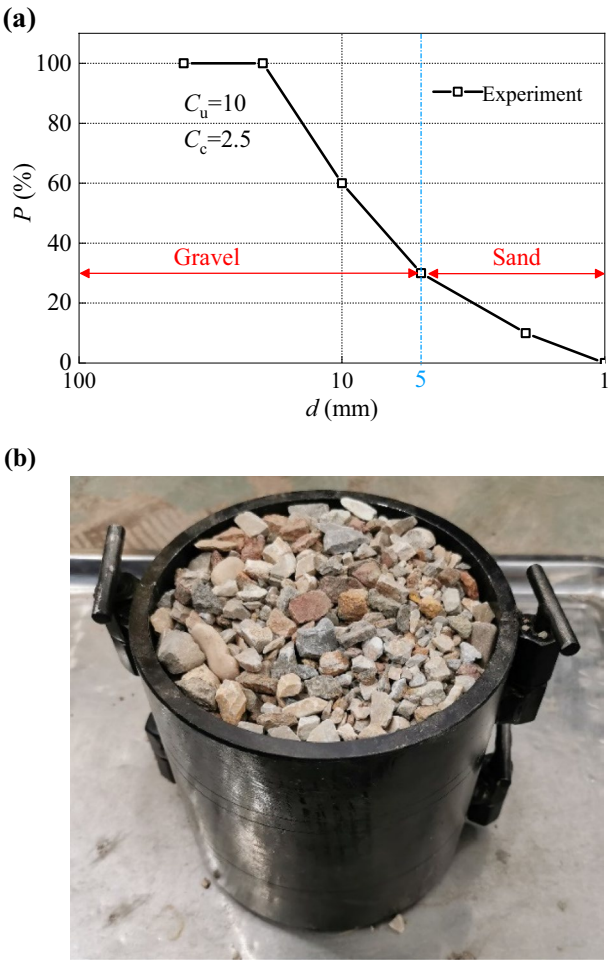

Fig. 1 Test materials: **a** gradation of filler; **b** container

complex images is of great importance for the subsequent particle morphology quantification, batch analysis, and discrete element numerical simulation.

Based on the previous studies, this paper first employs an improved Viola–Jones algorithm to automatically identify filler particles. The algorithm is simple, efficient, and accurate [50] and mainly includes four steps: (1) training dataset preparation, (2) training image resizing and rotation, (3) classifier training by AdaBoost and cascade, and (4) particle detection by the sliding window method. Next, the shape indexes are calculated, and a database of 2D filler aggregates is created. Finally, a discrete element model considering the particle shape and interparticle friction coefficient is established to analyze the static and dynamic meso-compaction characteristics of coarse-grained soil. The obtained results can be used to further explain the compaction mechanism for coarse-grained soil fillers.

2 Experimental study on realistic shapes

2.1 Test materials

Test materials were collected from the foundation filling section of the Beijing–Xiong'an intercity railway, China. Through a sieving test, four categories of filler aggregate particle sizes (1–2 mm, 2–5 mm, 5–10 mm, and 10–20 mm) are obtained. Considering the image pixels and the efficiency of discrete element calculation, the designed filler gradation is shown in Fig. 1a. Based on the grading curve, the uniformity coefficient $C_u = 10$ and curvature coefficient $C_c = 2.5$ are calculated according to their respective definitions [51]:

$$C_u = \frac{d_{60}}{d_{10}}, \tag{1}$$

$$C_c = \frac{d_{30}^2}{d_{60} d_{10}}, \tag{2}$$

where d_{10}, d_{30}, and d_{60} represent the particle sizes corresponding to the ordinate values of 10%, 30%, and 60%, respectively, on the grading curve.

In the test, the 1–2-mm and 2–5-mm particle groups are designated as fine particle groups, represented by the symbol 'S.' The 5–10-mm and 10–20-mm particle groups are denoted as coarse particle groups, represented by the symbol 'G.' To reduce the influence of impurities, the test filler particles were washed, dried, cooled, and then evenly stirred, after which they are freely packed in a custom-made iron container, as shown in Fig. 1b.

2.2 Automated extraction of the subgrade filler particles

2.2.1 Preparation of the training dataset

We have totally captured 1206 images of the filler samples, some of which are cropped, downscaled, and processed as the training dataset. The positive images are the complete outline of the filler aggregate particles, while the remaining images are marked as negative images. All the example images are 32 × 32 pixels in size. The computer learns from these data to determine the Haar-like feature in pattern recognition [50].

2.2.2 Training image resizing and rotation

Note that most natural subgrade filler particles exhibit an aspect ratio (AR) between 1:1 and 2:1. Hence, it is difficult to capture many such images through photography. Therefore, we need a new method to capture numerous images. To quickly record many elongated particle images for training, the existing particle images showing an AR of 1:1 are digitally stretched. The previous 1:1 training image (32 × 32 pixels) were resized to generate 1.5:1 training image (48 × 32 pixels), 2:1 training image (64 × 32 pixels), 3:1 training image (96 × 32 pixels), and 4:1 training image (128 × 32 pixels). Meanwhile, to recognize the elongated filler particles at any orientation, the original image is rotated counterclockwise in 15° increments. After rotating the images by 15°, 30°, 45°, 60°, 75°, 90°, 105°, 120°, 135°, 150°, and 165°, we acquire 13 rotated images. Simple samples at 0°, 30°, and 60° are shown in Fig. 2.

The next task is to combine all the results from these rotated images. In each image, if we successfully recognize the particles, we add a bounding box of these particles. All the bounding boxes are then superimposed, and

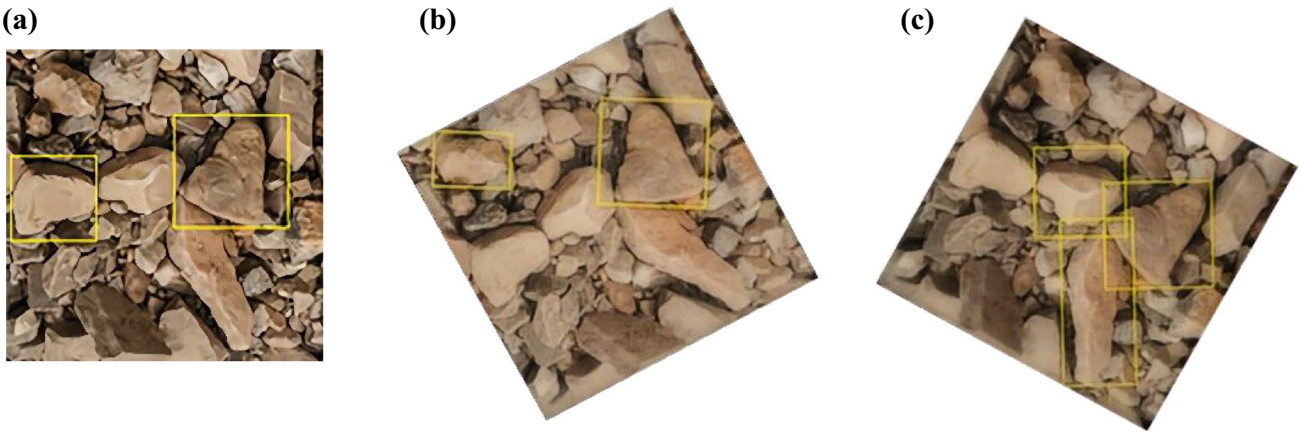

Fig. 2 Rotation of the original image: **a** 0°; **b** 30°; **c** 60°

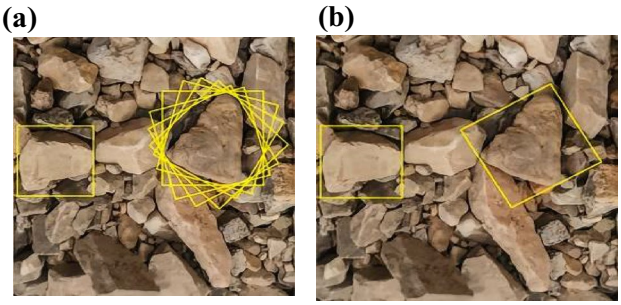

Fig. 3 Combined results of these images: **a** combined results of all rotations; **b** average particle window

certain boxes may be generated by the same particle due to the rotation. We then rotate the image to the original 0° position, and rotated sliding windows are obtained. Under these circumstances, we select the box with the minimum area as the final box of a given particle, as shown in Fig. 3.

2.2.3 Classifier training by AdaBoost and cascade methods

Subsequently, all the labeled images are employed to train the computer to compare the positive and negative images in the dataset, whereby the differences in features between the positive and negative images are retained. First, we apply the *AdaBoost* and *cascade* methods. Then, we recognize the particles using the sliding window method introduced in the next section.

AdaBoost is an algorithm that combines certain weak classifiers into strong classifiers. This strong classifier can be applied in the cascade method. A description of the algorithm is provided in Fig. 4. For a given value of T, the algorithm performs t=1, 2,..., T iterations. In the Tth iteration, we build the function $\hat{f}^t$ by applying the AdaBoost method considering the current weights ω_i. We compute the error err_t on the (weighted) training dataset, namely, the sum of the weights of all misclassified instances divided by the sum of all weights. If $eer_t = 0$ (i.e., the method is perfectly accurate on the training dataset) or if $eer_t \geq 0.5$, we then terminate the iterative process. Otherwise, for every correctly classified instance, the weight remains unchanged, while for every incorrectly classified instance, the weight is increased by a factor of $(1- eer_t)/eer_t$. At the end of the process, we return the combination of the classifiers for which the output of the tth classifier is weighted by $\log((1-eer_t)/eer_t)$. As such, in a given test instance, each $\hat{f}^t$ returns a probability distribution over two classes, and we combine these probabilities proportionally to the associated multipliers.

The cascade method divides the training process into several stages. In each stage, we train a strong classifier with the AdaBoost algorithm. We then specify three

Algorithm 1: AdaBoost

Set $\omega_i \leftarrow 1/n$, **for** $i = 1, 2, \cdots, n$.

for $t = 1, 2, \cdots, T$ **do**

  Apply learning method on weighted dataset to obtain model $\hat{f}^t$.

  $err_t \leftarrow \sum_{i=1}^{n} \hat{f}^t(x_i) \neq y_i \, \omega_i$

  if $0 < err_t < 0.5$ **then**, **for** all i:

  $$\omega_i \leftarrow \begin{cases} \omega_i & \text{if } \hat{f}^t(x_i) = y_i \\ \omega_i \dfrac{1-err_t}{err_t} & \text{if } \hat{f}^t(x_i) \neq y_i \end{cases}$$

  eles terminate.

  for all i, $\omega_i \leftarrow \omega_i / \sum_{i=1}^{n} \omega_i$. (Normalise)

return the function $\hat{f}(x) = \sum_{t=1}^{T} \log\left(\dfrac{1-err_t}{err_t}\right) \hat{f}^t$

Fig. 4 AdaBoost algorithm. $\hat{f}^t$ is a weak classifier, and $\hat{f}(x)$ is the final classifier

parameters, namely, the number of stages s, the detection rate d, and the false-positive rate f. In each stage, we search for the minimum T with the AdaBoost algorithm, and T must satisfy the requirement that the strong classifier $C(x)$ trained by the AdaBoost algorithm yields a detection rate higher than d and a false-positive rate lower than f.

Figure 5 shows the hypothetical example of the cascade method. The input data comprise 100 positive and 100 negative images. The original parameters are $s = 3$, $d = 0.99$, and $f = 0.25$ in each stage. A strong classifier is trained by the AdaBoost algorithm with a proper T value in each stage (T is assumed to be 3, 10, and 35 in stages 1, 2, and 3, respectively). In stage 1, we have 200 input images, and the classifier satisfies the requirement that the detection rate is higher than d, and the false-positive rate is lower than f. With $d = 0.99$ and $f = 0.25$, at least $100 \times 0.99 = 99$ images are correctly classified as positive images, while at most $100 \times 0.25 = 25$ images are misclassified. Hence, the classifier outputs 124 positive images, of which 99 are real particles and are taken as the input images in stage 2. All the other 76 images output as negative images is rejected. Via a similar calculation in stage 2, since we only have 99 positive images, the detection rate is thus 98/99 = 0.99, and the false-positive rate is 6/25 = 0.24, which satisfies the requirement. Subsequently, in stage 3, we obtain an output consisting of 98 images of 97 particles and one non-particle, and the detection rate is 97/98 = 0.99, with a false-positive rate of 1/6 = 0.17. Therefore, after the three ($s = 3$) stages, we obtain an overall detection rate of $D = d^3 = 0.97$ and an overall false-positive rate of $F = f^3 = 0.015$.

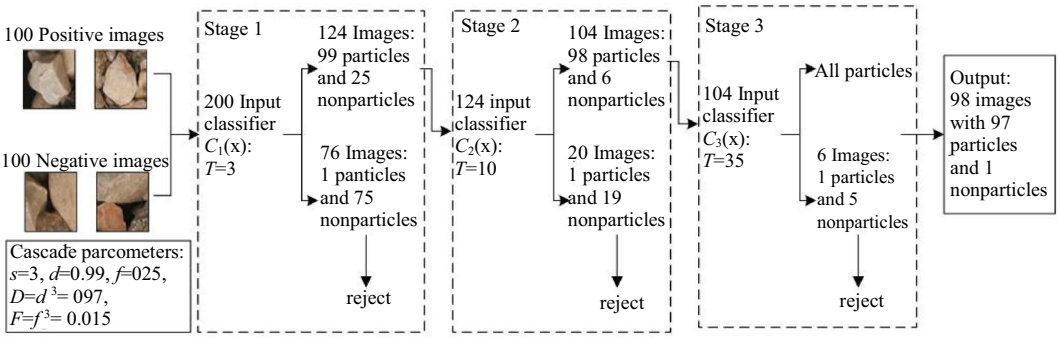

Fig. 5 A hypothetical example of the cascade method. s is the number of stages, d is the detection rate, f is the false-positive rate, and T is the number of iterations of the AdaBoost algorithm

2.2.4 Particle detection by the sliding window method

With the use of the previous classifiers, we obtain images containing real particles. The next task involves the recognition of full-projection particles. At each scanning location, the area within the sliding window is input into a detector. The detector extracts features from the window area based on which the classifier decides whether the image is positive or negative. If a positive image is determined, a bounding box is added at the scanning location, thus identifying it as an area containing full-projection particles. The specific process is explained below.

Since the minimum pixel size of a particle is 50×50, we first apply a 50×50 sliding window to scan the whole image. In each window, the image is cropped as the input to the classifier. Note that the previous classifiers are trained based on 32×32 images, and any cropped image larger than 32×32 must first be downscaled to 32×32 and tested by $C_{1(x)}$. If the output is positive, we then move to stage 2 in the cascade method. Otherwise, we reject the negative image, and the sliding window moves to the next position by 1 pixel. If the cropped image successfully passes all s classifiers, it is highly likely a positive image containing a full-projection particle. The sliding window at this position is then marked as a bounding box of this particle. Next, we continue to move the sliding window. Note that the movement increment is 1 pixel in both the horizontal and vertical directions, and the movement path is shown in Fig. 6a.

When the 50×50 sliding window successfully scans the whole image, we increase the size of the sliding window by 5 pixels in both directions, as shown in Fig. 6b. We repeat the previous sliding procedure until the sliding window is expanded to a maximum size of 300×300 pixels. It should be noted that most cropped images are classified as negative images and rejected, and only a few images pass all s classifiers, which is computationally efficient. In addition, when the sliding window is sufficiently large, several movements of the sliding window completely contain the particle and thus produce a bounding box. In this case, we calculate the average value, which can be adopted as a new single window.

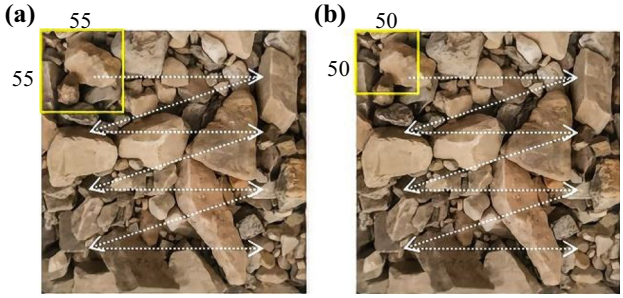

Fig. 6 Sliding window and movement path: **a** minimum sliding window; **b** sliding window increased by 5 pixels

2.3 Shape analysis and particle library establishment

With the full-projection particles acquired, particle shape parameters are computed following a series of computational geometry algorithms. The particle shape can be described through three geometrical scales, i.e., the form, roundness, and surface texture, as shown in Fig. 7.

2.3.1 Shape quantification index

As shown in Fig. 7, the first level shape index AR, denoted by R_a hereinafter, describes the overall radial dimensional scale characteristics of the particle outline and reflects whether the particle is close to circular in outline. For the spherical particles of the coarse-grained filler aggregate, the AR is equal to 1.

$$R_a = \frac{L}{S}, \tag{3}$$

where L is the length of the particle along the largest major axis, and S is the width along the smallest major axis.

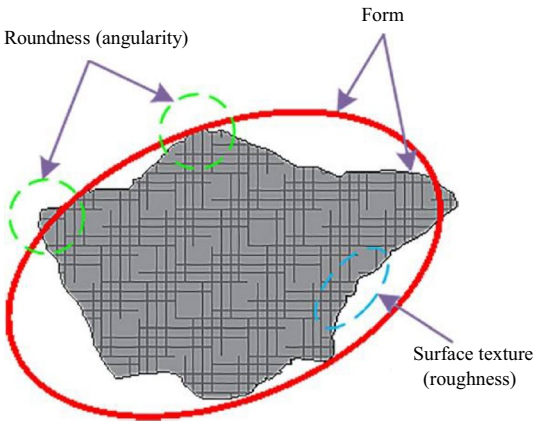

Fig. 7 Demonstration of the particle shape at the different levels

Additionally, the second level shape index, roundness (R_d), is mainly used to evaluate whether the corners of particles have smooth geometric characteristics:

$$R_d = \frac{\sum R_c}{n_c \cdot R_{insc}}, \tag{4}$$

where R_c is the radius of the local inscribed circle, n_c is the total number of corners areas, and R_{insc} is the radius of the largest inner tangent circle.

The third-order scale, also known as the roughness (R_g), reflects the shape irregularity superimposed on the corners and is also a property of the particle surfaces between the corners. The R_g is calculated as follows: The angle θ and polar diameter d in the polar coordinates are extracted from the decomposed particle contour. Next, the 2D particles are expanded into consecutive points corresponding to θ and d. Finally, the discrete points are transformed into smooth curves by the 'the locally weighted regression smoothing' (LOESS) method. The R_g of a 2D particle is calculated as follows:

$$R_g = \sqrt{\frac{1}{n}\sum_{i=1}^{n}(y_i - y_{i\text{ - LOESS}})^2}, \tag{5}$$

where n is the number of points on the 2D particle contour, y_i is the y-coordinate of point i on the contour, and $y_{i\text{ - LOESS}}$ is the y-coordinate of point i after smoothing.

2.3.2 Shape statistics and particle library

First, we make a quantitative analysis of the 2D particle shape index from the particle library; the results are shown in Fig. 8.

As shown in Fig. 12a, the distribution of the roundness is between 0.2 and 0.4. The highest frequency is approximately

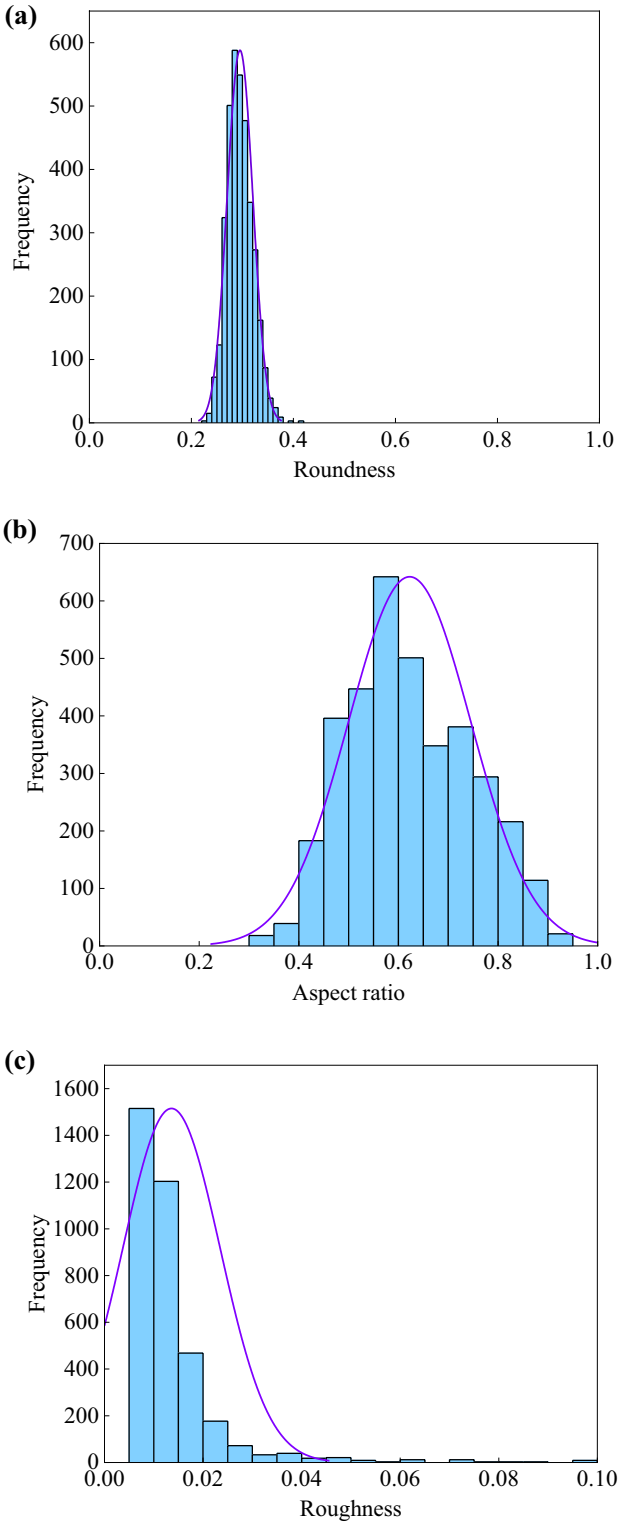

Fig. 8 Statistical distributions of the shape parameters: **a** roundness; **b** aspect ratio; **c** roughness

580, whose roundness is close to 0.28. In addition, the average roundness is approximately determined as 0.3 based on the fitting curve. Regarding the AR (Fig. 12b), its

distribution is between 0.2 and 1.0; the highest frequency of approximately 642 is achieved when AR approaches 0.575. Comparing the fitting curve to the horizontal axis values, we can see that the average AR is approximately 0.6. From the distribution of the roughness (Fig. 12c), it is obvious that most of the roughness data are concentrated at approximately 0.01, indicating that the particles are highly smooth. According to the fitting curve, the average roughness is approximately 0.02.

By comparing the differences between the distributions of the roundness, AR, and roughness, we find that the AR has the widest frequency range and hence fluctuates the most. The fluctuation in the roundness is the second highest, with its distribution mainly concentrated between 0.2 and 0.4. The change in roughness seems imperceptible, which is reflected in the narrow value variation range.

The shape indexes of the filler aggregate particles are stored with the coordinates of the outline point of the filler aggregates, which are stored in the format of [*X, Y*]. The storage format is [number, contour, R_a, R_d, R_g]. The following steps are taken to import the filler aggregate particle outlines into the particle flow code (PFC) software:

- First, the ranges of the desired shape parameters are input.
- Then, 2D contours that meet the requirements are automatically searched by the range of these values.
- Finally, visualized 2D contours are selected, and they are output as .dxf files.

After the particle library is established, it is convenient to select 2D outlines of filler particles that meet certain requirements to facilitate the discrete element modeling of filler materials, which contributes to the study of the relationship between the shape properties and compaction characteristics.

3 Static compaction DEM simulation

In this paper, PFC 2D 5.0 is adopted for modeling purposes, which is regarded as a reliable tool to study the mechanism and characteristics of the filler aggregates from a microscopic perspective [30]. Considering the computational efficiency of the DEM and the skeleton effect of coarse particles, the real shape of coarse particles of the filler aggregates (G) is simulated, and the fine particles (S) are simplified as spherical particles [52].

3.1 Sample preparation

The particle–particle and particle–wall interactions were modeled using the linear contact model, which can reproduce the compaction characteristics of the non-adhesive filler aggregates [28, 52–54]. The microscale parameters adopted in the DEM are summarized in Table 1, and all the microscale parameters have been previously validated [52, 55].

Figure 9 shows the generation process of the compacted sample, including particle generation, natural accumulation, and smoothing. Finally, 5028 non-overlapping particles are generated in the upper area of the container. Figure 10 shows the gradation distribution of the sample in the simulation. The coarse particle shape is characterized by $1/R_a$ (here $1/R_a$=1.25, 1.5, 1.75, and 2.0), which is prevalent in the shape library of the filler aggregate, as shown in Fig. 11.

After the particle system is established, gravitational acceleration is applied to the particles to ensure that they freely fall under the action of gravity. To improve the calculation efficiency, the local damping value is set to 0.7, and the global damping value is set to 0. The particle system then freely accumulates at the bottom of the container.

The initial height of the container is $40d_{max}$ and the initial width is $15d_{max}$, where d_{max} is the maximum equivalent particle diameter. Hence, the size effect is reduced in the experiment [56–58]. Finally, a clump is used to simulate a rigid pressure plate structure, and a static load is applied to the pressure plate clump.

3.2 Static compaction simulation

To clarify the load stress range in the model, a laboratory static compaction test was conducted (Fig. 12a). Uniaxial compression testing of coarse-grained soil was performed with a universal testing machine. A round iron plate (φ = 148 mm) slightly smaller than the inner diameter of the specimen was applied for loading. The compression deformation (mainly controlling the compression distance) of the soil samples was measured in the uniaxial compression test.

Table 1 Microscale parameters

Parameter	Value
Particle density (kg/m^3)	2650
μ (particle–particle)	0.2, 0.4, 0.6, and 0.8
μ (particle–wall)	0.12
K_n (fine particle–fine particle) (N/m)	1×10^8
K_n (coarse particle–coarse particle) (N/m)	5×10^8
K_n (coarse particle–coarse particle) (N/m)	3×10^8
K_n (particle–wall) (Pa)	1×10^9
Stiffness ratio, K_n/K_s	4/3
Damping factor	0.7

Note: μ is friction coefficient; K_n and K_s are normal and tangential contact stiffness, respectively

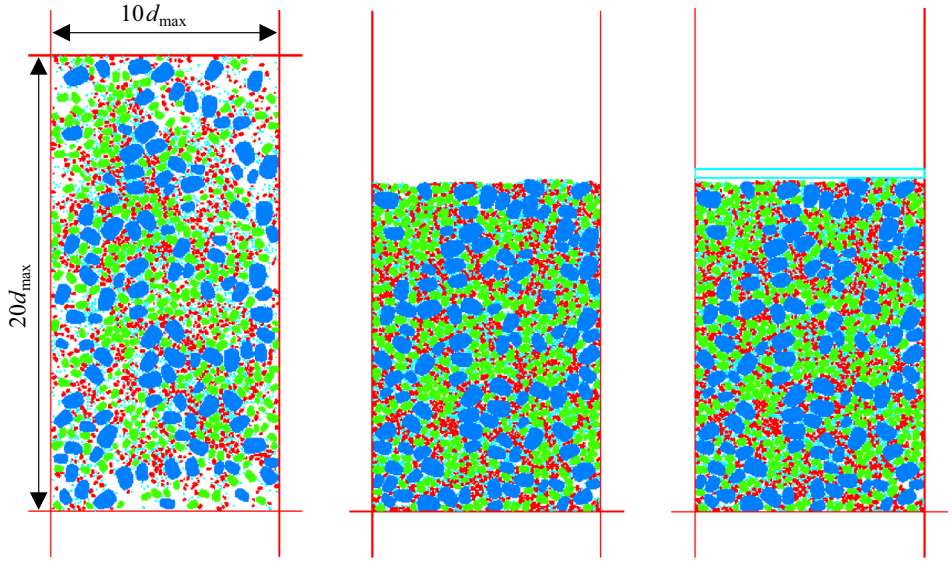

Fig. 9 Specimen generation

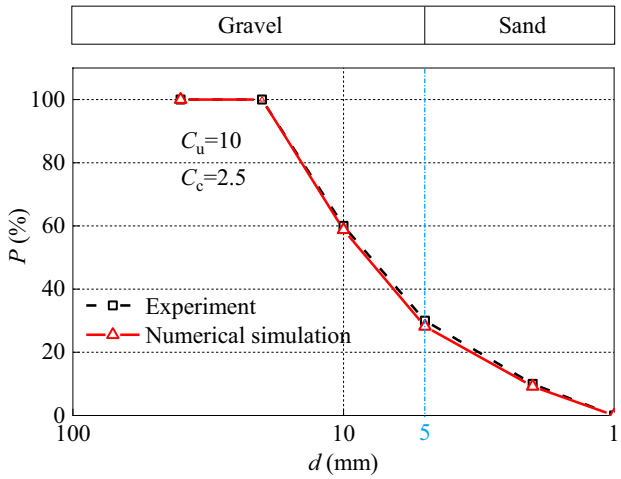

Fig. 10 Coarse particle size distribution

Figure 12b shows the results of the uniaxial compression test. The test curve can be divided into the following three stages by compression stress (σ):

- The first stage: σ= 1–50 kPa, the fast compaction step of the loose subgrade filler. Particles quickly fill the pores, and mainly plastic deformation occurs.
- The second stage: σ= 50–190 kPa, the subgrade filler elastic compression stage. The particles are squeezed and become interlocked, while primarily elastic deformation occurs.
- The third stage: σ> 190 kPa. The subgrade filler is broken and quickly compacted, and mainly plastic deformation occurs.

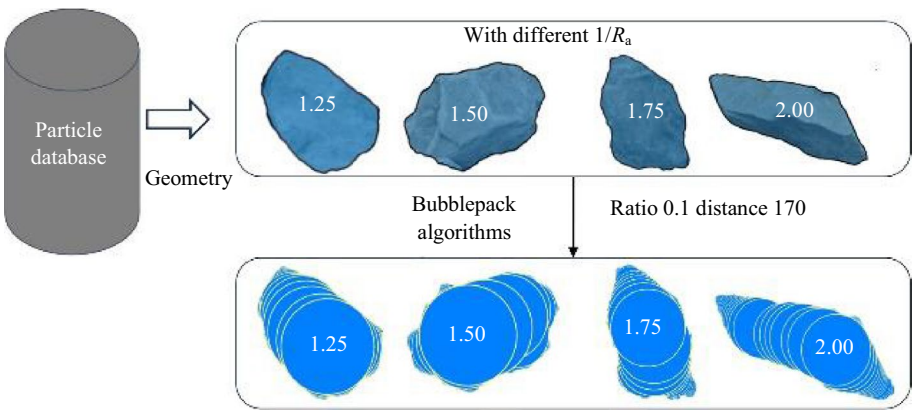

Fig. 11 Coarse particles with different $1/R_a$ values

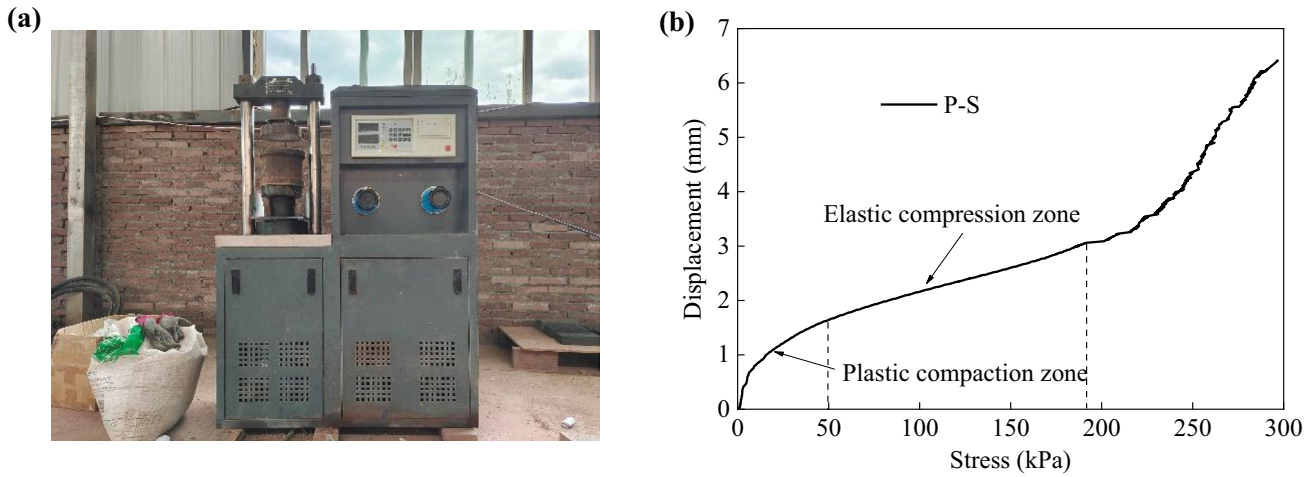

Fig. 12 Uniaxial compression test: **a** experimental procedure; **b** test results

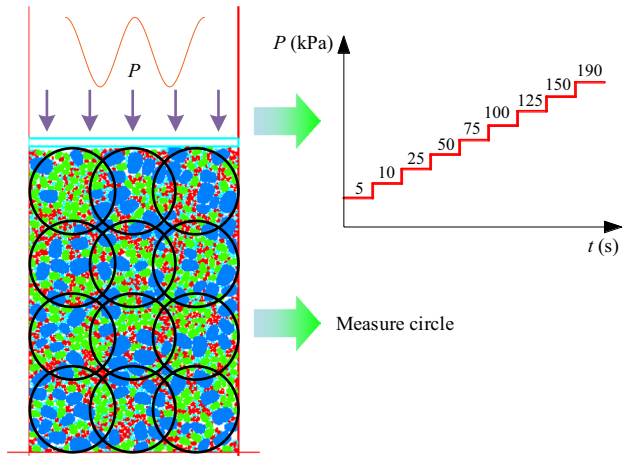

Fig. 13 Static load application

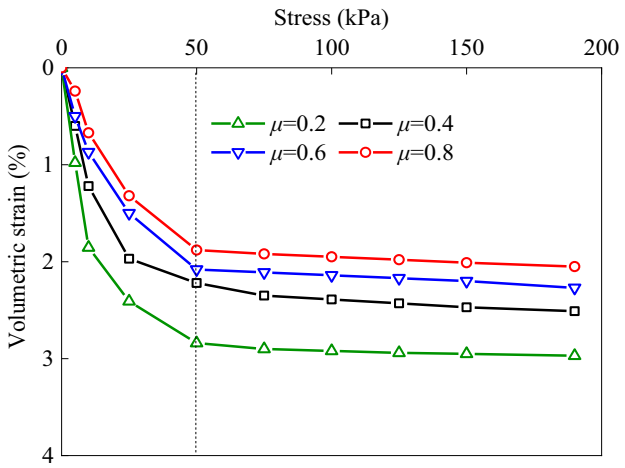

Fig. 14 Volumetric strain curves under different μ values ($1/R_a = 1.5$)

In the DEM simulation, the test load conditions are fully considered, as shown in Fig. 13. Under quasi-static loading, the kinetic energy generated by the particles during the loading process is negligible.

3.3 Influence of the imposed static loading

Figure 14 shows the relationship between the volumetric strain θ and compression stress σ ($1/R_a$ =1.5) for coarse-grained soil under different μ values. As the friction coefficient μ between the particles decreases, the specimen becomes increasingly dense. The value of θ under u= 0.2 is 50% higher than under u= 0.8. This is because that at the low u, the particle easily slips and rearranges.

The volumetric strain of the sample first notably increases with the compressive stress and then gradually stabilizes under compressive stress higher than 50 kPa. When the stress ranges from 0 to 50 kPa, the volumetric strain sharply increases. The particles in the sample become rearranged, fine particles are compressed into the pore spaces between large particles, and the loose structure gradually becomes more compact. In particular, the lower the μ value, the larger the slippage between the particles, the more the pore spaces become filled, and the higher the sample volumetric strain.

As the stress exceeds 50 kPa, the volumetric strain remains unchanged, and the particles are mainly extruded. In the calculation, the particles are set to be unbreakable, and this paper does not conduct research on the compression state above 50 kPa. The experimental and numerical results reveal that the compression stress of 50 kPa is the inflection point of the volumetric strain, which also indicates that the particle shape and calculation parameters of the model are accurate and reasonable.

The mean coordination number is defined as in Eq. (6), which was adopted to investigate the particle arrangement. The internal structure of the specimen was evaluated by the means of three traditional coordination numbers [52, 55]:

$$Z_{GG} = \frac{2N_{GG}}{N_G}, Z_{SS} = \frac{2N_{SS}}{N_S}, Z_{GS} = \frac{2N_{GS}}{N_G}, \tag{6}$$

where the subscripts 'G' and 'S' stand for gravel and sand, respectively; Z_{GG} is the average number of gravel particles around each gravel particle; Z_{SS} is the average number of sand particles around each sand particle; Z_{GS} is the average number of sand particles around each gravel particle; N_{GG} is the number of gravel particles around gravel particles; N_{SS} is the number of sand particles around sand particles; N_{GS} is the number of sand particles around gravel particles; and N_G, N_S, and N_G are the total number of gravel, sand, and gravel particles, respectively.

The contribution of a specific contact type k, i.e., C_k, can help to quantify the effect of different contact types on the resistance to an external load [52]. By analyzing the contribution of contact type k during the compaction process, we determine the force skeleton of the mixture changes [56, 58]. The contribution of different contact types to the external load resistance can be quantified, which has been previously verified [52, 55]. The contribution of contact type k can be written as follows:

$$C_k = \sigma_{ij}^k \Big/ \sigma_{ij}, \tag{7}$$

$$\sigma_{ij} = \frac{1}{V}\sum_{c\in N} f_i^c l_j^c, \tag{8}$$

where σ_{ij}^k is the macroscale stress tensor of contact type k; f_i^c is the ith component of the contact force at contact c, l_j^c is the jth component of the contact vector $\boldsymbol{l}_j$ at contact point c, N is the contact number in the specimen, and V is the volume of the specimen. Hence, the stress tensor can be divided into three sub-tensors based on contact type k.

The variation in the coordination number and contribution ($1/R_a = 1.5$, $\mu = 0.4$) is shown in Fig. 15. Figure 15a shows the evolution of the coordination number in different loading stages. The Z_{GS} value greatly exceeds the Z_{SS} and Z_{GG} values. As stress increases, the Z_{SS} value gradually exceeds the Z_{GG} value. The main reason is that after the granular material is compressed, fine particles are compressed into the pore spaces between coarse particles, resulting in the external load being borne by more fine particles. Under a pressure higher than 50 kPa, the particles are compacted, and the coordination number remains stable. A small amount of unstable coarse particles are compressed by the fine particles, which is clearly shown in Fig. 15b. The C_{GS} and C_{SS} values gradually increase with the increasing stress and remain stable in the later period. However, the C_{GG} value exhibits the opposite trend, gradually decreasing with the increasing load in the early stage and remaining stable in the later stage.

3.4 Influence of the shape and contact friction

The interparticle friction coefficient μ (0.2, 0.4, 0.6, and 0.8) [59] was varied to investigate the effects of the particle shape ($1/R_a = 1.25$, 1.5, 1.75, and 2.0) on the compaction analysis at the different void ratios e. The void ratio e is defined as follows:

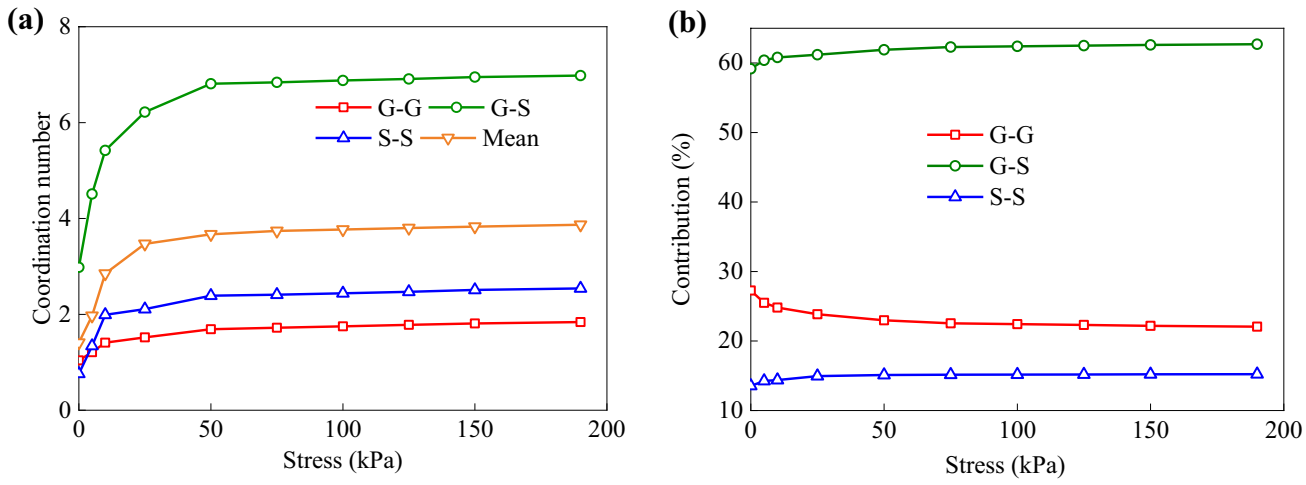

Fig. 15 Variation in the coordination number and contribution ($1/R_a = 1.5$): **a** coordination number of the different contact types; **b** contribution of the different contact types

$$e = \frac{V - V_p}{V_p}, \tag{9}$$

where V_p is the volume of particles.

The distribution of the void ratio e is shown in Fig. 16. With the μ value increasing, the e value gradually increases, but the rate of increase gradually decreases. However, as the $1/R_a$ value increases, the e value gradually increases. It is observed that the narrower the particles are, the more pores occur between the particles during natural accumulation under the action of self-weight compaction, and the more unstable the structure is. The volumetric strain of the granular material with $\sigma = 50$ kPa is shown in Fig. 17. With the μ value decreasing, the $1/R_a$ value increases, and the granular material experiences greater deformation. Under μ=0.8, the volumetric strain of the granular material remains basically unchanged.

Figure 18 shows the evolution of the mean coordination number. The mean coordination number of all assemblies exhibits a decreasing trend with the μ value increasing. This indicates that increasing μ will lead to a reduction in the number of contacts at the contact point. Under σ= 50 kPa, the lower the $1/R_a$ value, the smaller the contact number, and the contact number decreases with μ increasing.

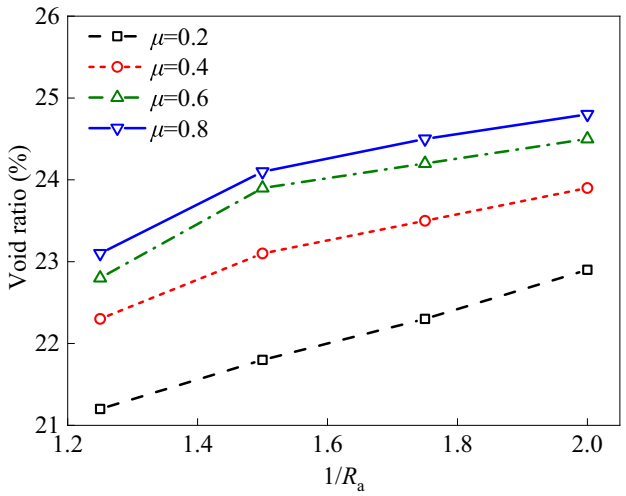

Fig. 16 Void ratio versus the $1/R_a$ value under different interparticle friction coefficients in the initial state

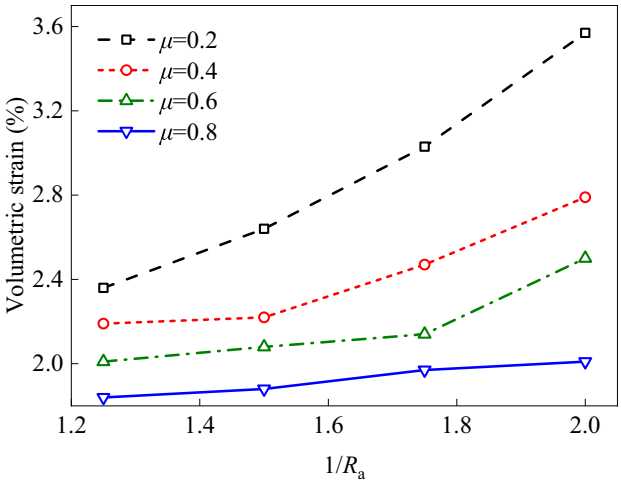

Fig. 17 Volumetric strain versus the $1/R_a$ value under different interparticle friction coefficients (σ=50 kPa)

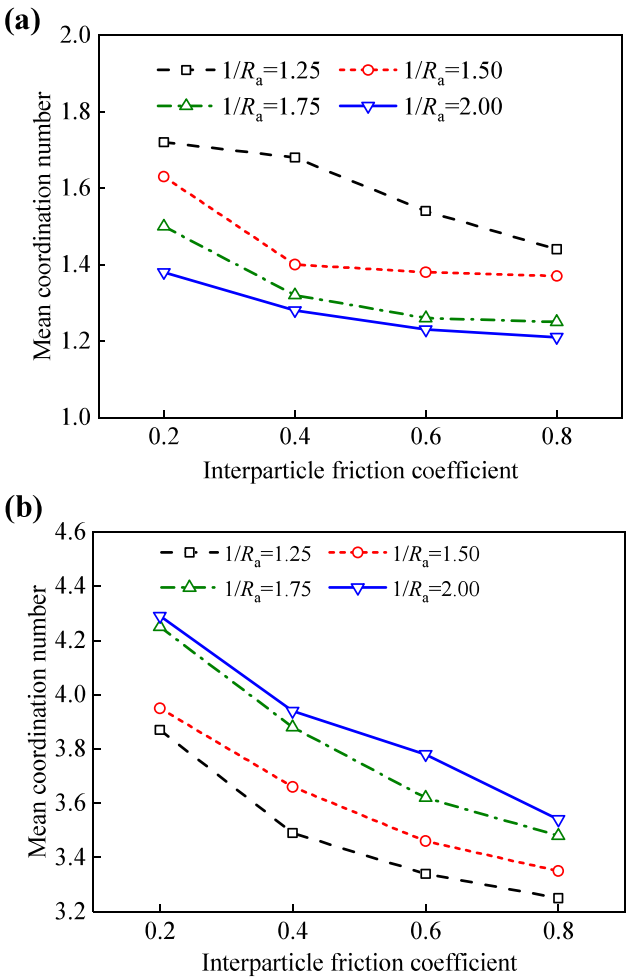

Fig. 18 Volumetric strain versus the interparticle friction coefficient at the different $1/R_a$ values: **a** σ = 0 kPa; **b** σ =50 kPa.

4 DEM simulation of vibration compaction

Vibration compaction is the movement of particles under a vibration load, which may increase the packing density. Applying vibration loads with different frequencies, we study the real shape particle movement and change in dry density and provide a new research idea for the determination of the compaction mechanism of coarse-grained soil.

4.1 Sample preparation

The discrete element model is basically the same as the uniaxial compression model. However, considering the vibration load, the global damping level of all particles was set to 0.1 [60, 61]. A static load was then applied to the pressure plate, the main purpose of which is to ensure that the pressure plate fully contacts the surface of the filler particles. Finally, a vibration load was applied to the pressure plate. The dynamic loads applied in the model were determined by experiments.

4.2 Simulation of the vibration compaction test

To determine the method to apply the vibration load, a TLD-ZDY-type vibration compactor (Fig. 19a) was adopted to conduct a vibration compaction test. The change in dry density with the vibration frequency can be roughly divided into two steps. In the first step, the coarse-grained soil increases slowly over the vibration frequency range from 10 to 15 Hz, and in the second step, the

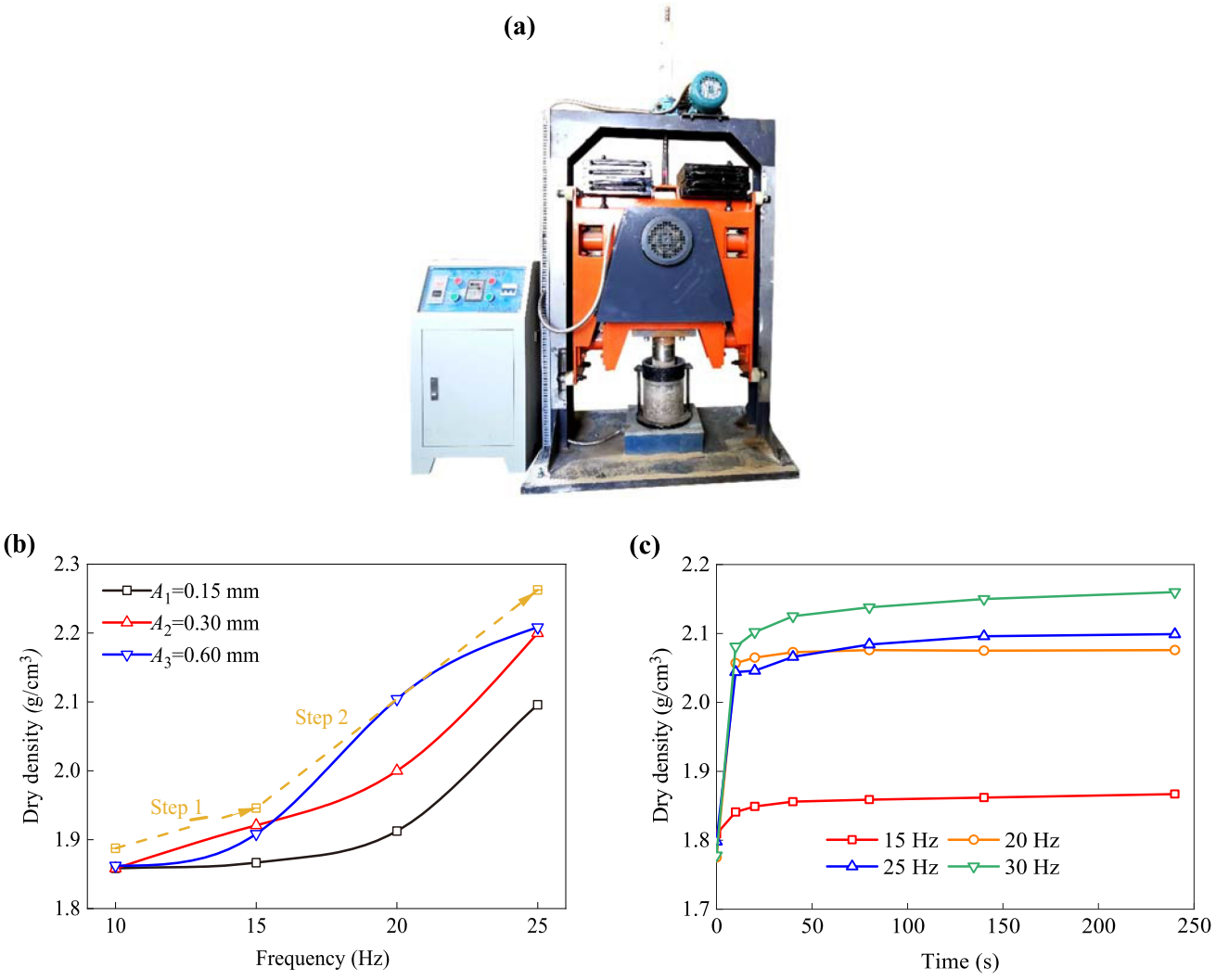

Fig. 19 Vibration compaction test: **a** vibration compactor; **b** dry density versus vibration frequency for different vibration amplitudes (A_1, A_2, and A_3); **c** dry density versus time for different vibration frequencies with 0.3-mm magnitude

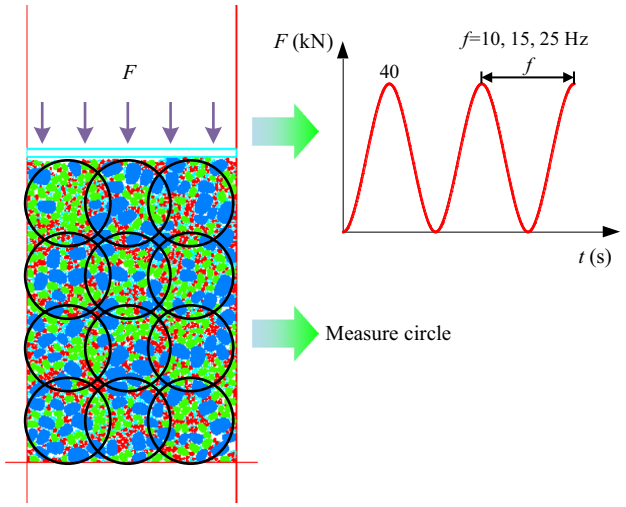

Fig. 20 Dynamic load application

coarse-grained soil is rapidly compacted over the vibration frequency range from 16 to 25 Hz.

Using the CLUMP command of PFC software, a top mass–wall boundary was developed. As shown in Fig. 20, a boundary of 10-mm thickness was generated by overlapping pebbles, which have a density the same as the steel tamper (7800 kg/m^3). An excitation force F, which varies with time t, is applied to the mass–wall model through a FISH script. The applied force F can be calculated as follows:

$$F = F_{\max} \sin(2\pi f t), \tag{10}$$

where $F_{\max}$ is the maximum excitation force, f is the vibration frequency, and t is time. In the simulation, the vibration frequencies are set to 10, 15, 20, and 25 Hz, and the maximum excitation force is set to 40 kN. The macro- and mesoscopic characteristics of the vibration compaction within 10 s are analyzed.

4.3 Influence of the shape and frequency on the particle motion

The vibration velocity of the coarse particles (G) and fine particles (S) is shown in Fig. 21a. Under the action of the vibration load, the vibration velocity of the coarse particles is low, while the vibration velocity of the fine particles is high. The higher the $1/R_a$ value is, the higher the vibration frequency and velocity of the fine particles are. The main reason is that more internal pores exist among particles with higher $1/R_a$ values, which allow freer movements of the fine particles. At high vibration frequencies, the fine particles tend to move more easily. The coarse particles mainly function as a skeleton, and their change is small with increasing $1/R_a$ value and vibration frequency. The particle positions are rearranged, and the particles tend to approach each other, which, in turn, increases the packing density. The average displacement of the coarse and fine particles at $f = 25$ Hz is shown in Fig. 21b. Obviously, the higher the $1/R_a$ value, the larger the average displacement of the particles. Moreover, the increasing aspect ratio of the coarse particle leads to the increasing movement of fine particles. This phenomenon reflects that it is difficult for slender coarse particles to inhibit the migration of fine particles. More irregular particles are, therefore, more prone to relative sliding between particles, resulting in larger vertical displacements of particles.

Rotation is an important motion of particles under external load. Figure 22 shows the average rotation of

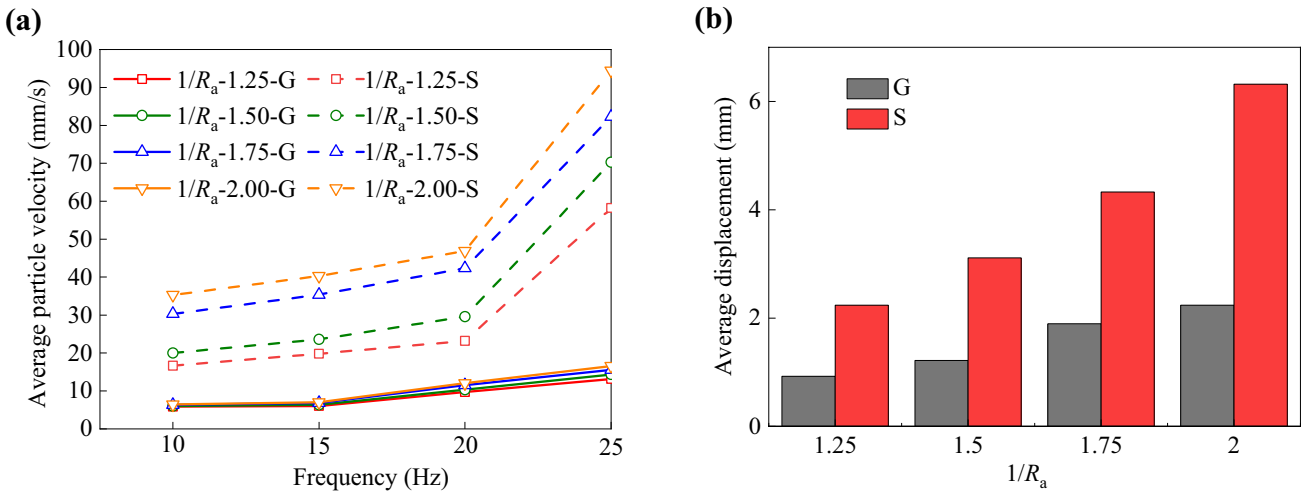

Fig. 21 Particle movement: **a** average particle velocity; **b** average vertical displacement (f = 25 Hz)

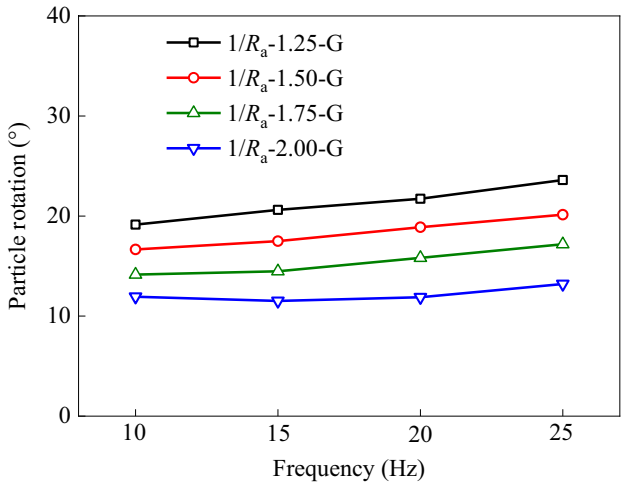

Fig. 22 Particle rotation versus frequency at the different $1/R_a$ values

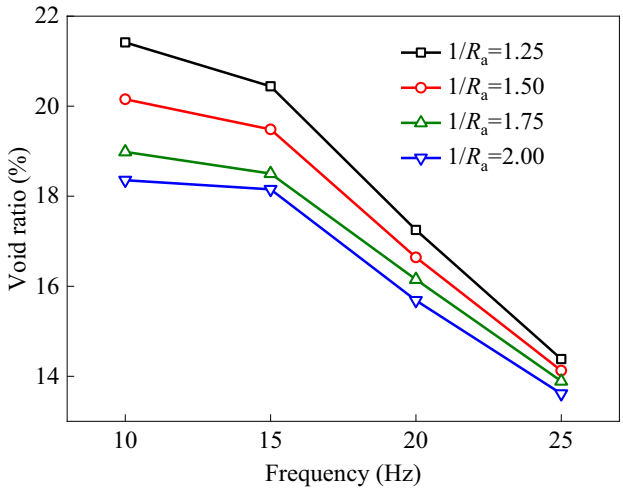

Fig. 23 Void ratio versus frequency at the different $1/R_a$ values

coarse particles after compaction. For a specific $1/R_a$, the rotation of the coarse increases with increasing frequency, and the gradient increases gradually. In addition, slender particles are more difficult to rotate than round ones. That is, consistent with static conditions, slender particles have stronger anti-rotation ability compared to round particles under dynamic load.

4.4 Influence of the shape and frequency on the void ratio

The discrete element model established in this paper does not consider the effect of water and assumes the same density for the coarse and fine particles. Therefore, Eq. (9) holds; i.e., the dry and mixture densities are equal.

$$\rho_d = \frac{m}{V} = \frac{\rho_s V_s}{V} = \rho_s \frac{V - V_v}{V} = \rho_s(1 - n), \tag{11}$$

where ρ_d is the dry density, m is the particle mass, ρ_s is the density of the solid particles, V is the total volume, V_s is the volume of the solid particles, V_v is the pore volume, and n is the porosity.

Equation (9) indicates that with porosity increasing, the dry density of the sample linearly decreases; i.e., the dry density and porosity are linearly related. In the vibration compaction test, the maximum dry density is adopted to evaluate the compaction quality. In the discrete element model, since the dry density exhibits a linear relationship with the porosity, the porosity can be adopted to evaluate the compaction quality of the simulation test.

The relationship between the compaction degree of particles with different shapes (indicated by the void ratio) and the vibration frequency is shown in Fig. 23. Similar to the test results, the compaction degree slowly increases under low-frequency vibration loads. As the vibration frequency increases from 15 to 25 Hz, the compaction degree increases rapidly. In addition, the compaction degree increases with an increase in the $1/R_a$ value of particles, but compaction effect caused by increasing the $1/R_a$ value diminish gradually with the vibration frequency increasing. When the vibration frequency is 25 Hz, the compaction degree of particles for all $1/R_a$ values is nearly the same.

The relationship between the compaction degree and frequency under the different friction coefficients (μ=0.2, 0.4, 0.6, and 0.8) for the subgrade filler ($1/R_a$=1.5) is shown in Fig. 24. The friction coefficient exerts little effect on compaction. The calculation result is similar to that reported in Refs. [60, 61]. Although the friction coefficient of the coarse-grained soil gradually increases, due

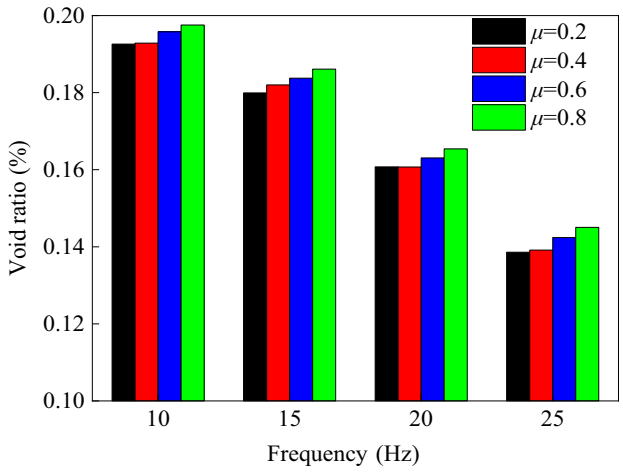

Fig. 24 Void ratio versus frequency under the different friction coefficients

to the impact of the vibration load, the friction resistance between the filler particles is reduced notably, and the dynamic friction coefficient between the soil–rock mixture particles remains relatively similar.

5 Discussion

Filler particle materials are nonlinear systems with complex geometrical characteristics, and it is a challenging scientific problem to quantify the effect of particle shape on the compaction characteristics of fillers. This paper focuses on the effect of particle AR on the compaction characteristics of the filler. Compared to static compaction, the effect of particle roughness under dynamic action is substantially weakened, so that compaction under dynamic action is not based on slippage. Under vibratory compaction, the effect of vibration frequency on the rotation of particles with different aspect ratios is not significant, indicating that the mechanisms of dynamic compaction are also not particle rolling. However, the mean particle displacement is influenced by the particle AR, suggesting that it is influenced by particle shape under dynamic occlusion. Meanwhile, the displacement and velocity of the fine particles are much greater than that of the coarse particles, indicating that compaction is primarily a migration of the fine particles.

In this paper, the effects of vibration parameters and friction between filler particles on the particle motion during vibratory compaction of filler are mainly investigated, while the analysis of the forces on the particles at different AR is lacking. At the same time, further in-depth explanation of the compaction mechanism requires the development of a 3D model. Future work involves the extension into 3D space, as shown in Fig. 25. A certain number of coarse-grained soils will be selected and scanned by the 3D laser scanning technology to obtain the 3D sharpness of the coarse-grained soil particles. The actual gradation of the particles will then be determined via image processing, and coarse-grained soil particles of different particle sizes will be imported into the DEM according to the actual gradation. Moreover, the interlocking conditions and dynamic mechanical response between the different coarse-grained soil particles will be investigated.

6 Conclusions

This paper applies the DEM to study the micromechanical compaction characteristics of coarse-grained soil. An improved Viola–Jones algorithm is adopted to automatically identify coarse filler particles. A particle library is established based on the three types of particle shape indexes. Finally, by recalling particles at different $1/R_a$ values from the particle library, numerical simulations are conducted to quantitatively investigate the effects of the AR and interparticle friction coefficient on the macro- and micro-mechanical compaction characteristics of the subgrade filler via PFC 2D. The main conclusions are as follows:

1. With an increasing $1/R_a$ value, the particles are narrower, the void ratio increases, and the mean coordination number exhibits a decreasing trend. For different particle shapes, the friction coefficient of particles does not affect the static compaction load when the volumetric strain of the sample reaches stability, and the internal structure is stable under the same static compaction load.
2. According to the average displacement of particles under cyclic load, the increasing aspect ratio of the coarse particle leads to the increasing movement of fine particles. In other word, it is difficult for slender coarse particles to inhibit the migration of fine particles.
3. The interparticle friction coefficient has different influences on the internal structure of the specimen under cyclic and quasi-static loads. In general, under a cyclic load, μ has little effect on the internal structure of the

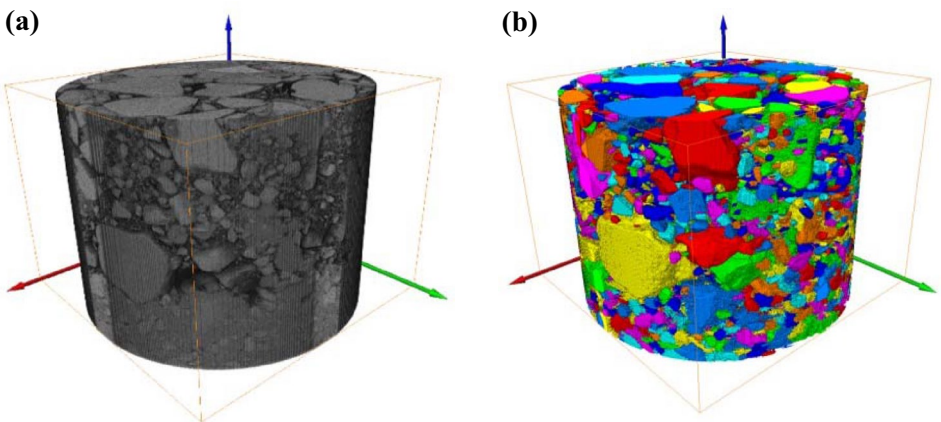

Fig. 25 Three-dimensional model of coarse-grained soil

sample. However, under the quasi-static loads, the increase in μ will lead to a significant increase in the porosity of the sample.

4. The small effect of vibration frequency on particle rotation indicates that the mechanism of dynamic compaction is not particle rolling. The average displacement of particles is strongly influenced by the aspect ratio, and therefore, the occlusion under power relies on shape. The displacement and velocity of fine particles are much greater than those of coarse particles, indicating that compaction is primarily a migration of fine particles.

Acknowledgments This work was supported by the National Key R&D Program 'Transportation Infrastructure' project (No. 2022YFB2603400).

References

1. Gautier PE (2015) Slab track: review of existing systems and optimization potentials including very high speed. Constr Build Mater 92:9–15
2. Steenbergen MJMM, Metrikine AV, Esveld C (2007) Assessment of design parameters of a slab track railway system from a dynamic viewpoint. J Sound Vib 306(1–2):361–371
3. Huang JJ, Su Q, Cheng YM et al (2019) Improved performance of the subgrade bed under the slab track of high-speed railway using polyurethane adhesive. Constr Build Mater 208:710–722
4. Huang J, Su Q, Liu T et al (2019) Behavior and control of the ballastless track-subgrade vibration induced by high-speed trains moving on the subgrade bed with mud pumping. Shock Vib 2019:1–14
5. Li T, Su Q, Kaewunruen S (2020) Seismic metamaterial barriers for ground vibration mitigation in railways considering the train-track-soil dynamic interactions. Constr Build Mater 260:119936
6. Nie R, Dong J, Leng W, et al (2020) Backbone curve model of saturated coarse-grained soil under train-induced cyclic loading. In: Advances in environmental vibration and transportation geodynamics. Lecture Notes in Civil Engineering, Springer, Singapore, pp 763-778.
7. Wan Z, Bian X, Li S et al (2020) Remediation of mud pumping in ballastless high-speed railway using polyurethane chemical injection. Constr Build Mater 259:120401
8. Song W (2012) Research on mechanical property and constitutive mode of coarse-grained soils. Dissertation, Central South University (in Chinese)
9. Ye Y, Cai D, Yao J et al (2021) Review on dynamic modulus of coarse-grained soil filling for high-speed railway subgrade. Transp Geotech 27:100421
10. Hu YF (2010) Design principles of ballastless track subgrade of high-speed railway. China Railway Press, Beijing (in Chinese)
11. Wang X, Dong X, Zhang Z et al (2022) Compaction quality evaluation of subgrade based on soil characteristics assessment using machine learning. Transp Geotech 32:100703
12. Isik F, Ozden G (2013) Estimating compaction parameters of fine- and coarse-grained soils by means of artificial neural networks. Environ Earth Sci 69(7):2287–2297
13. Qian Q, An X, Wang Y et al (2016) Physical study on the vibrated packing densification of mono-sized cylindrical particles. Particuology 29:120–125
14. Xie Z, An X, Wu Y et al (2017) Experimental study on the packing of cubic particles under three-dimensional vibration. Powder Technol 317:13–22
15. Xu P, Zhu X, Qiao S et al (2022) Field study of compaction quality control parameters and compaction mechanism of large particle size stone-filled embankment. Rock Mech Rock Eng 55(6):3687–3702
16. Zhang Q, An Z, Huangfu Z et al (2022) A review on roller compaction quality control and assurance methods for earthwork in five application scenarios. Materials 15(7):2610
17. Zhao Y, Xie S, Gao Y et al (2021) Prediction of the number of roller passes and degree of compaction of asphalt layer based on compaction energy. Constr Build Mater 277:122274
18. Seif El Dine B, Dupla JC, Frank R et al (2010) Mechanical characterization of matrix coarse-grained soils with a large-sized triaxial device. Can Geotech J 47(4):425–438
19. Xu GH, Gao H, Wang ZR (2005) Analysis of continuous dynamic monitoring on vibrating compaction process of graded broken stone. Chin J Geotech Eng 27(11):1270–1272 (in Chinese)
20. Duong TV, Cui YJ, Tang AM et al (2016) Effects of water and fines contents on the resilient modulus of the interlayer soil of railway substructure. Acta Geotech 11(1):51–59
21. Mooney MA, Gorman PB, González JN (2005) Vibration-based health monitoring of earth structures. Struct Heath Monit 4(2):137–152
22. Sakai H, Nordfjell T, Suadicani K et al (2008) Soil compaction on forest soils from different kinds of tires and tracks and possibility of accurate estimate. Croat J for Eng 29:15–27
23. Ye Y, Cai D, Tian S et al (2023) Experimental investigation of the particle breakage of coarse-grained materials under impact loading. Transp Geotech 40:100954
24. Mostofinejad D, Reisi M (2012) A new DEM-based method to predict packing density of coarse aggregates considering their grading and shapes. Constr Build Mater 35:414–420
25. Qian G, Hu K, Li J et al (2020) Compaction process tracking for asphalt mixture using discrete element method. Constr Build Mater 235:117478
26. Xu D, Tang Z, Zhang L (2019) Interpretation of coarse effect in simple shear behavior of binary sand-gravel mixture by DEM with authentic particle shape. Constr Build Mater 195:292–304
27. Zhao L, Zhang S, Huang D et al (2020) A digitalized 2D particle database for statistical shape analysis and discrete modeling of rock aggregate. Constr Build Mater 247:117906
28. Nie Z, Zhu Y, Zou J et al (2019) DEM study of the microscopic characteristics and internal stability of binary mixtures. Powder Technol 352:314–324
29. Shire T, O'Sullivan C (2013) Micromechanical assessment of an internal stability criterion. Acta Geotech 8(1):81–90

30. Gong J, Liu J (2017) Mechanical transitional behavior of binary mixtures via DEM: effect of differences in contact-type friction coefficients. Comput Geotech 85:1–14
31. Guo Y, Zhao C, Markine V et al (2020) Calibration for discrete element modelling of railway ballast: a review. Transp Geotech 23:100341
32. Härtl J, Ooi JY (2011) Numerical investigation of particle shape and particle friction on limiting bulk friction in direct shear tests and comparison with experiments. Powder Technol 212(1):231–239
33. Yang Y, Cheng YM, Wang JA (2016) Exploring the contact types within mixtures of different shapes at the steady state by DEM. Powder Technol 301:440–448
34. Mora CF, Kwan AKH, Chan HC (1998) Particle size distribution analysis of coarse aggregate using digital image processing. Cem Concr Res 28(6):921–932
35. Fernlund JMR (2005) Image analysis method for determining 3-D shape of coarse aggregate. Cem Concr Res 35(8):1629–1637
36. Maerz N, Zhou W (1999) Flat and elongated: advances using digital image analysis. In: Center for aggregates research (ICAR) Seventh annual symposium proceedings, Austin Texas, April 19-21
37. Descantes Y, Fosse Y, Milcent F (2006) Automated measurement of railway ballast angularity. J Mater Civ Eng 18(4):612–618
38. Al-Rousan TM (2004) Characterization of aggregate shape properties using a computer automated system. Dissertaion, Texas A&M University.
39. Al-Rousan T, Masad E, Tutumluer E et al (2007) Evaluation of image analysis techniques for quantifying aggregate shape characteristics. Constr Build Mater 21(5):978–990
40. Blott SJ, Pye K (2007) Particle shape: a review and new methods of characterization and classification. Sedimentology 55(1):31–63
41. Kwan AKH, Mora CF, Chan HC (1999) Particle shape analysis of coarse aggregate using digital image processing. Cem Concr Res 29(9):1403–1410
42. Tafesse S, Robison Fernlund JM, Sun W et al (2013) Evaluation of image analysis methods used for quantification of particle angularity. Sedimentology 60(4):1100–1110
43. Vangla P, Roy N, Gali ML (2017) Image based shape characterization of granular materials and its effect on kinematics of particle motion. Granul Matter 20(1):1–19
44. Zhang D, Huang X, Zhao Y (2012) Investigation of the shape, size, angularity and surface texture properties of coarse aggregates. Constr Build Mater 34:330–336
45. Zheng J, Hryciw RD (2015) Traditional soil particle sphericity, roundness and surface roughness by computational geometry. Géotechnique 65(6):494–506
46. Zheng J, Hryciw RD (2016) Roundness and sphericity of soil particles in assemblies by computational geometry. J Comput Civ Eng 30(6):04016021
47. Guo Y, Markine V, Zhang X et al (2019) Image analysis for morphology, rheology and degradation study of railway ballast: a review. Transp Geotech 18:173–211
48. Liang Z, Nie Z, An A et al (2019) A particle shape extraction and evaluation method using a deep convolutional neural network and digital image processing. Powder Technol 353:156–170
49. Zheng J, Hryciw RD (2018) Identification and characterization of particle shapes from images of sand assemblies using pattern recognition. J Comput Civ Eng 32(3):110–121
50. Freund Y, Schapire RE (1995) A desicion-theoretic generalization of on-line learning and an application to boosting. In: Vitányi P (ed) Computational Learning Theory. EuroCOLT 1995, vol 904. Lecture Notes in Computer Science. Springer, Berlin
51. National Railway Administration of the People's Republic of China (2016) Code for design of railway subgrade. TB10001-2016. China Railway Publishing House, Beijing (in Chinese)
52. Gong J, Nie Z, Zhu Y et al (2019) Exploring the effects of particle shape and content of fines on the shear behavior of sand-fines mixtures via the DEM. Comput Geotech 106:161–176
53. Lopera Perez JC, Kwok CY, Senetakis K (2017) Effect of rubber content on the unstable behaviour of sand–rubber mixtures under static loading: a micro-mechanical study. Géotechnique 68(7):561–574
54. Wang C, Deng A, Taheri A (2018) Three-dimensional discrete element modeling of direct shear test for granular rubber-sand. Comput Geotech 97:204–216
55. Liu D, Sun L, Ma H et al (2020) Process simulation and mesoscopic analysis of rockfill dam compaction using discrete element method. Int J Geomech 20(6):04020047
56. Abbireddy COR, Clayton CRI (2010) Varying initial void ratios for DEM simulations. Géotechnique 60(6):497–502
57. Li X, Yu HS (2013) Particle-scale insight into deformation noncolatility of granular materials. Int J Geomech 15(4):04014061
58. Yang J, Dai BB (2012) Is the quasi-steady state a real behavior? A micromechanical perspective. Géotechnique 62(5):466–468
59. Suhr B, Six K (2020) Simple particle shapes for DEM simulations of railway ballast: influence of shape descriptors on packing behaviour. Granul Matter 22:43
60. El Shamy U, Denissen C (2012) Microscale energy dissipation mechanisms in cyclically-loaded granular soils. Geotech Geol Eng 30(2):343–361
61. Zhang Y, Liu Z, Shi C et al (2018) Three-dimensional reconstruction of block shape irregularity and its effects on block impacts using an energy-based approach. Rock Mech Rock Eng 51(4):1173–1191